IEEE Access
Multidisciplinary | Rapid Review | Open Access Journal

Received 6 June 2023, accepted 13 August 2023, date of publication 17 August 2023, date of current version 28 November 2023.

Digital Object Identifier 10.1109/ACCESS.2023.3305968

METHODS

Optimized Parking Control for Electric Vehicle Driven by Switched Reluctance Motor

PEILIN LIU, TAO WANG, (Member, IEEE), ZHIYUAN CHAI, CHUANG LIU, AND XUEZHONG ZHU

College of Automation Engineering, Nanjing University of Aeronautics and Astronautics, Nanjing 211106, China

Corresponding author: Chuang Liu (liuchuangnuaa@163.com)

This work was supported in part by the National Natural Science Foundation of China under Project 51877108 and 52207059, National Key Laboratory of Science and Technology on Helicopter Transmission under Grant HTL-A-22K02.

ABSTRACT Sufficient and stable positioning torque is necessary for the parking of an electric vehicle driven by switched reluctance motor (SRM). Considering the highly nonlinear torque characteristic of SRM, the parking control with high stability and power consumption economy is an important issue. This paper presents an optimized parking control method for an electric vehicle driven by SRM to achieve optimal parking stability and power consumption economy simultaneously. The static torque-angle characteristic curve of a four-phase 16/12 SRM is analyzed, based on which the optimized region of parking position (presented by rotor angle) is obtained considering the uncertainty of parking conditions. To ensure the vehicle is properly parked in the optimized position region, active disturbance rejection control (ADRC) is utilized to achieve the smooth switch from zero-speed control to parking position control. Simulation and experimental results verify that the proposed method can better stabilize the parking on the ramp and reduce power consumption in all conditions.

INDEX TERMS Switched reluctance motor (SRM), optimized parking method, active disturbance rejection control (ADRC), parking power consumption.

I. INTRODUCTION

The parking brake system of an electric vehicle usually requires coordination between mechanical components and drive motors [1], [2], [3]. However, for some electric construction machinery (such as excavators, earthmovers, mining trucks, forklifts, etc.), the aforementioned mixed parking brake system faces the following challenges [4], [5]:

1) Electric construction machinery needs frequent start-and-stop on tough roads, which is challenging for the coordinated control between mechanical components and drive motors.
2) Problems such as wear and fatigue caused by the frequent use of mechanical components threaten the parking safety of electric construction machinery.
3) The coordination control of mechanical and electrical components depends on a high level of vehicle automation, which is difficult to achieve on low-cost electric construction machinery.

Therefore, the research on parking control of electric construction machinery solely depending on drive motors has potentially high engineering application value. In fact, this type of parking control has been applied in G series electric forklifts cooperated by HELI (see Fig. 1), an international construction machinery enterprise, and ZAPI, a vehicle controller manufacturer. Although this function sacrifices a part of power consumption compared with the mechanical components-involved way, it is beneficial to frequent start-and-stop under complex conditions and reduces mechanical braking components' wear and fatigue.

Existing mass-produced electric construction machinery, such as Komatsu's electric forklift [6], [7], Hitachi's hybrid electric wheel loader [8], and the hybrid electric excavator of Case and Sumitomo [9], etc., is driven mainly by AC motors (induction or synchronous ones). Their solely motor-based parking control is easy to achieve for the mature control techniques of induction and synchronous motors.

The associate editor coordinating the review of this manuscript and approving it for publication was Jorge Esteban Rodas Benítez.

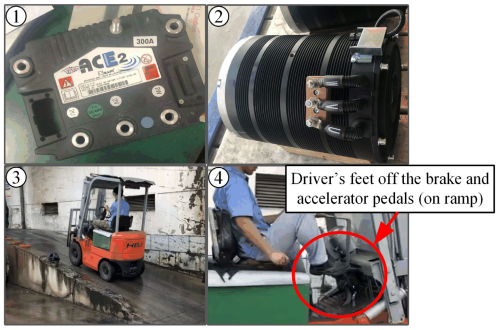

①Three phase drive machine controller (supplied by ZAPI)
②Three phase induction machine (serve the drive system)
③Electric forklift (supplied by HELI) parking on ramp
④Test of machine-independent parking control

FIGURE 1. Parking function achieved solely depending on drive motor.

With the development of switched reluctance motor (SRM) technology for vehicles, such as optimization of electromagnetic performance [10], [11], [12], [13], [14], [15], vibration and noise reduction [16], [17], [18], [19], [20], [21], and torque ripple optimization [22], [23], [24], [25], [26], [27], [28], SRM has shown great application value in electric construction machinery. However, due to the highly nonlinear

torque characteristic and special control method of SRM, the solely motor-based parking control of electric construction machinery driven by SRM is a tricky problem, which still lacks in-depth research, and few related reports can be found at the moment.

The main contributions of this paper are as follows:

1) A novel research on the solely motor-based electric vehicle parking control strategy of SRM is presented for the first time. The objective of this research is to optimize the stability and power efficiency of parking.
2) By analyzing the nonlinear torque characteristic of the SRM and the direction of the rolling resistance torque, the optimized range of rotor angle is determined for stability and efficiency improvement when parking on ramps. But for flats, only no power consumption should be achieved.
3) ADRC is employed to achieve accurate rotor angle control, and a seamless switching logic between zero-speed control and parking position control is proposed for the first time.

This article is organized as follows. Section II analyses the power consumption and stability of the solely motor-based parking based on the static torque-angle characteristic curve of the SRM and the rolling resistance. Section III analyses and designs the optimized parking method, including the zero-speed control and the parking position control. In section IV and V, simulation and experimental test results are both carried out to validate the effectiveness and merit of the proposed parking control strategy. Section VI discusses the main advantages and disadvantages of the optimized parking method and presents potential future research. Section VII concludes this article.

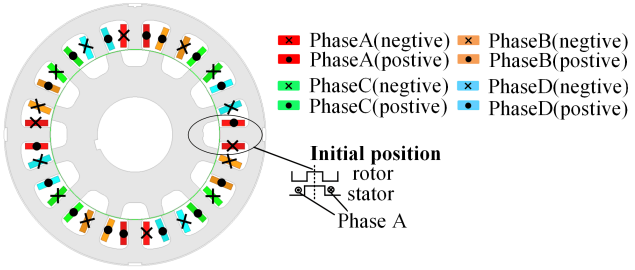

FIGURE 2. Topology of four-phase 16/12 SRM in this paper.

II. ANALYSIS OF FOUR-PHASE 16/12 SWITCHED RELUCTANCE MOTOR FOR ELECTRIC VEHICLE PARKING

Through the structural design of SRM for electric vehicles in [11], considering the dynamic performance, this paper adopts a four-phase 16/12 SRM as the drive system of the electric vehicle, whose topology is shown in Fig. 2.

A. ANALYSIS OF PARKING BRAKE SYSTEM BASED ON SRM STATIC TORQUE-ANGLE CHARACTERISTIC

Apart from the dynamic process of parking control, the fully parked vehicle can be regarded as a static state (called ''final parking state''). Hence, the static torque-angle characteristic analysis of the SRM is essential. If only considering the grade resistance torque (T_i) and electromagnetic torque (T_e), Fig. 3(a) shows the three typical parking conditions against which the SRM needs to generate the corresponding T_e ($|T_e| = |T_i|$, especially on the flat: $|T_e| = |T_i| = 0$).

According to the control logic of four-phase SRM, SRM still keeps two phases conducted in the final parking state. Through the finite element simulation, Fig. 3(b) shows the static torque-angle characteristic curve of the conducted two phases (A&B) displayed at 100A, 70A and 40A, respectively. Moreover, Fig. 3(c) shows the single direction of periodic positive and negative torque through the control logic. The logic for square wave current conduction in finite element simulation is shown in appendix.

Due to the highly nonlinear torque characteristic of SRM, the T_e under the final parking state has a significant periodic ripple. Some issues with the parking brake system need to be considered.

1) The T_e fluctuates greatly with the rotor angle under the same current. In other words, the rotor angle when the vehicle is fully parked (called ''fully parked rotor angle'') determines the parking power consumption.
2) The gradient characteristic of T_e and rotor angle ($d(T_e)/d(\theta)$) has two polarities. Moreover, the fully parked rotor angle may determine the parking stability.

B. DEFINITION OF IDEAL PARKING REGION BASED ON ANALYSIS OF PARKING POWER CONSUMPTION AND STABILITY

In order to achieve efficient and stable parking, the ideal parking region (the expected range of rotor angle when the

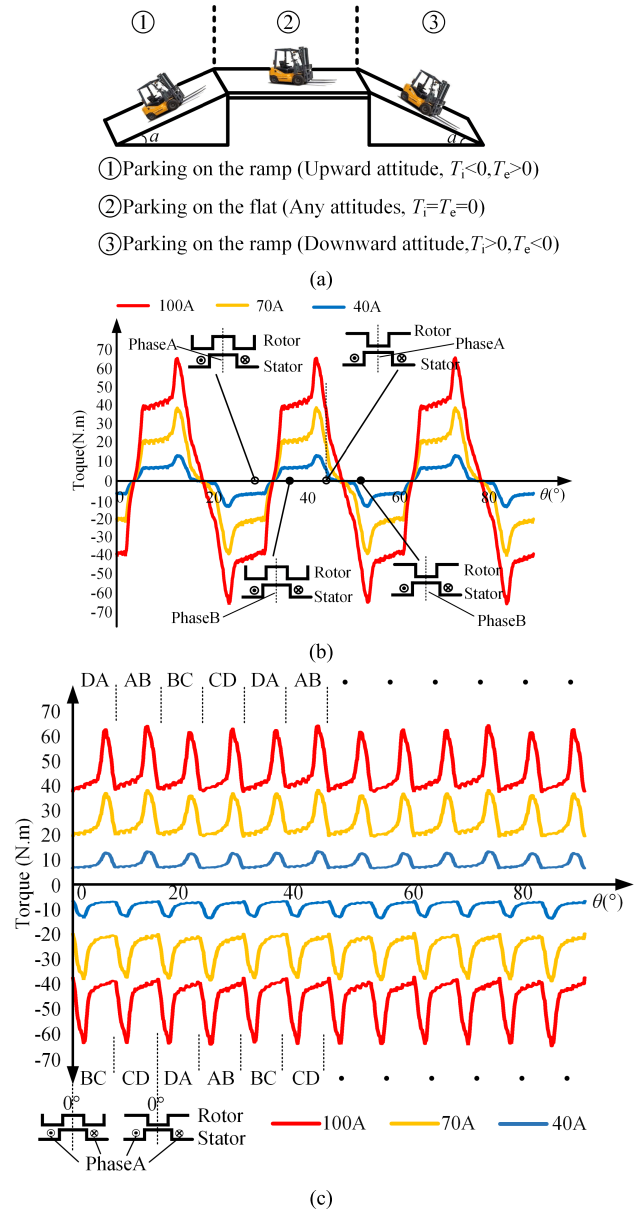

FIGURE 3. Analysis of parking brake system based on SRM static torque-angle characteristic. (a) Relationship among T_e, T_i, and parking conditions. (b) Static torque with the adjacent different two phases conducted. (c) Static torque with the adjacent same two phases (A&B) conducted.

vehicle is fully parked) is defined based on the static torque analysis of SRM. This region leads to less power consumption and better parking stability.

Fig. 4 shows the simplified static torque-angle characteristic, according to three obvious gradient change points (θ_i, θ_h, θ_m), the simplified curve is divided into three segments (called "region" in the following parts, region i: $\theta_i \sim \theta_h$; region ii: $\theta_h \sim \theta_m$; region iii: $\theta_m \sim \theta_i$). The period of the curve is theoretically derived as 7.5° (1/4 electrical period). For parking on the ramp, T_e is non-zero and produces a certain copper loss on phase windings. For a specific ramp, affected by the inherent torque ripple of the SRM shown in Fig. 3(c),

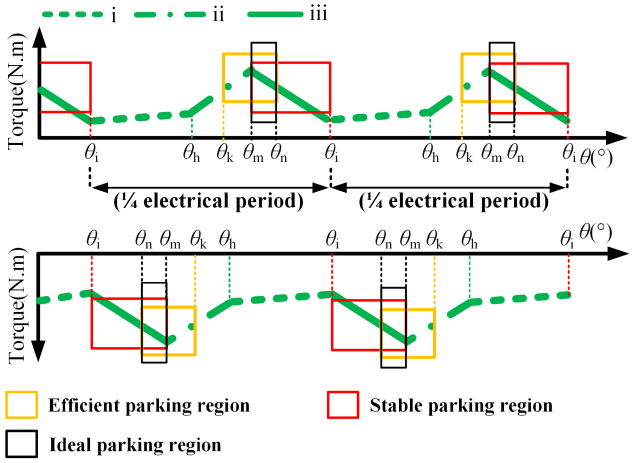

FIGURE 4. The definition of ideal parking region.

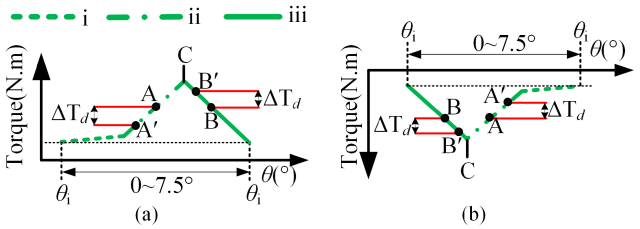

FIGURE 5. Analysis of parking stability (a) $T_e > 0$. (b) $T_e < 0$.

different copper loss may be produced when the fully parked rotor angle is different. For less copper loss of parking on the same ramp, yellow rectangular boxes shown in Fig. 4 are used to select the regions with huge amplitude of the curve (called efficient parking region: $\theta_k \sim \theta_n$).

Assuming that the balance between T_e and T_i is achieved in the efficient parking region, but there are two types of lines in this region ($\theta_k \sim \theta_m$: $d(T_e)/d(\theta) > 0$; $\theta_m \sim \theta_n$: $d(T_e)/d(\theta) < 0$). To observe the system's parking stability, a disturbance (ΔT_d) is applied in the same direction as T_i after fully parked. In Fig. 5(a). Points A and B are all in the efficient parking region with static state shown in Fig. 4. Due to the existence of ΔT_d, the rotor moves in the negative direction. When the ΔT_d disappears, the rotor is at point A'. At this time, T_e does not balance T_i. The system will be farther away from the balance point. But for point B, under the same change of ΔT_d, the torque-angle characteristic can make the rotor return from point B' to point B. Fig. 5(b) can be analyzed as the same.

In conclusion, $d(T_e)/d(\theta) < 0$ is the necessary condition for weighing parking stability. As a result, the red rectangular boxes shown in Fig. 4 are used to select the regions with properties of $d(T_e)/d(\theta) < 0$ (called stable parking region: $\theta_m \sim \theta_i$).

As a result, according to the definition of efficient and stable parking regions for parking on the ramp, the ideal parking region ($\theta_m \sim \theta_n$) can be defined as the overlapping part of the two regions. Although point C has the best economy of

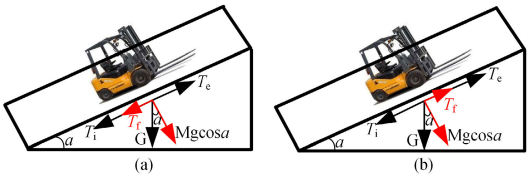

FIGURE 6. Analysis of rolling resistance torque. (a) T_i and T_f are in the same direction. (b) T_e and T_f are in the same direction.

power consumption, it has apparent defects from the parking stability. Some overshoot may cause the system to enter an unstable region (region ii). Therefore, the rotor angle distance between θ_m and θ_n cannot be reduced blindly to pursue the ultimate power consumption.

But for parking on the flat ($T_i = 0$), the SRM system does not need to provide T_e under the final parking state. Hence, there is no copper loss in the phase windings, and parking stability analysis does not exist. Moreover, the angle of the final parking state on the flat may no longer be constrained by the definition of the regions mentioned above.

C. POWER CONSUMPTION OPTIMIZATION BASED ON ANALYSIS OF ROLLING RESISTANCE TORQUE

To analyze the parking brake system more accurately, this section adds rolling resistance torque (T_f) into the parking analysis by ignoring air drag for low speed conditions regarding the research of general vehicles [25].

As shown in Fig. 6, where a is the gradient, and f_r is the rolling resistance coefficient of the tire and road surface. Considering the T_f as the property of the friction resistance torque, the T_f is used to balance the vector sum of the T_i and the T_e in the final parking state. In contrast, the T_f is determined by the f_r and the tire-to-ground pressure in the moving state.

Under the final parking state, T_e, T_i, and T_f shall meet:

$$T_e + T_i + T_f = 0. \tag{1}$$

With the same final parking state, if the amplitude of T_e generated by motor is greater than the amplitude of T_i, there must exist a rolling resistance torque T_f in the opposite direction to T_e, as shown in Fig. 6(a). Similarly, if the amplitude of T_e is smaller than the amplitude of T_i, there must exist a T_f in the same direction as T_e, as shown in Fig. 6(b). Combining these two cases, based on (1), two typical relationships can be derived, as shown in (2) and (3).

$$T_e sign\left(T_e\right) = T_i sign\left(T_i\right) + T_f sign\left(T_f\right). \tag{2}$$

$$T_i sign\left(T_i\right) = T_e sign\left(T_e\right) + T_f sign\left(T_f\right). \tag{3}$$

As a result, if the direction of the T_f is adjusted to satisfy (3), the parking model performs better in power consumption (less amplitude of T_e) through the optimized parking control.

But for $T_i = 0$ (parking on the flat), for the perfect power consumption, T_f should be reduced to 0N.m through the optimized parking control.

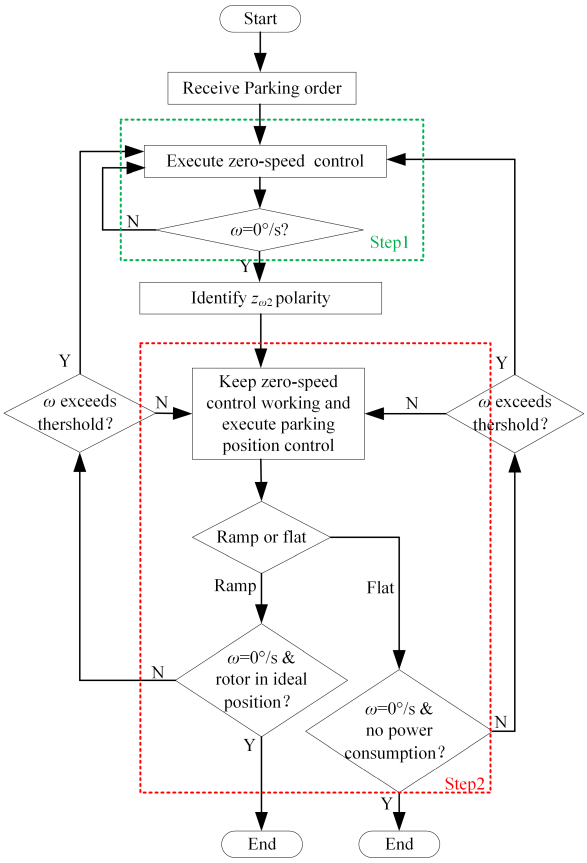

FIGURE 7. Flow chart of the optimized parking control method.

D. SUMMARY

As a result, based on the analysis of SRM torque characteristics and the types of parking conditions, the desired outcome of the optimized parking control is to achieve the ideal parking region with the rotor moving in the specified direction on the ramp, and to achieve no power consumption while maintaining a stationary state on the flat.

III. OPTIMIZED PARKING CONTROL

A. ANALYSIS OF OPTIMIZED PARKING CONTROL

Since parking control is a process that involves decelerating the rotor from any initial speed to a final speed of 0°/*s*, regardless of whether the system is parked on the ramp or flat, the process can be divided into two steps:

Step 1: Make the drive motor reach 0°/*s* through speed control (called "zero-speed control").

Step 2: Move the rotor to the corresponding ideal parking region through position control (called "parking position control").

Fig. 7 shows the flow chart of the optimized parking control method. **Step 1** and **Step 2** are executed when the system receives the parking order. The purpose of zero-speed control operating in the whole method is to ensure that the system can be protected in case of the parking position control stall. Moreover, ω_0 and θ_0 are set as the target value of zero-speed

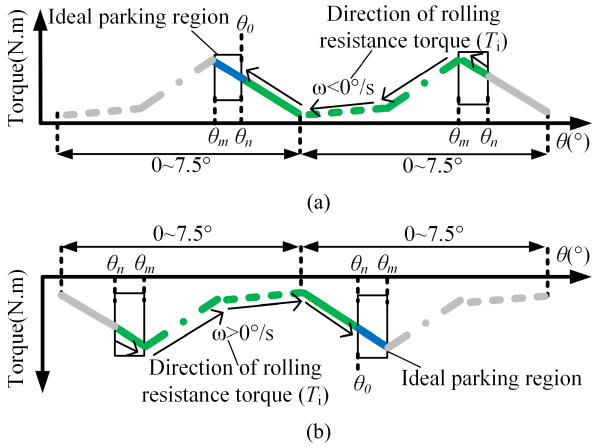

FIGURE 8. Direction of parking position control. (a) $T_e > 0$. (b) $T_e < 0$.

control and parking position control, respectively. For zero-speed control, ω_0 is a fixed value ($0°/s$). But for parking position control, due to the periodicity of the static torque-angle characteristic, θ_0 needs to find an angle point in the corresponding ideal parking region after **Step 1**.

As shown in Fig. 7, after **Step 1,** the parking control process changes due to the different parking conditions.

1) PARKING ON THE RAMP

a) The T_i direction should be taken as the position control direction, whether the vehicle is in an upward or downward attitude on the ramp. As a result, the angular speed of the rotor entering the ideal parking region is 0°/s, ensuring the final Tf is in the same direction as the Te according to (3). As the actual process overshoots are inevitable, for more stability, θn is selected as the target value (θ0) through the direction of Ti, as shown in Fig. 8.

b) After **Step 1**, the rotor's initial angle may already be in the ideal parking region. As the direction of T_f is unknown at this time, θ_0 still need to be set as the target value in the adjacent ideal parking region, shown in Fig. 8.

c) Since the vehicle is not fitted with ramp detection devices, after **Step 1**, the system requires an observation to judge the T_i, which is crucial to select the θ_0 for the parking position control.

2) PARKING ON THE FLAT

a) Since the T_i is 0N.m, T_f will be generated by parking position control in any direction after **Step 1**. In this case, the SRM has no practical ideal parking region. The control objective is to reduce the phase winding current to 0A and achieve no power consumption stationary.

b) Due to (1), even if $a > 0$, it can also be considered as a flat condition as long as T_f can fully offset T_i.

c) Since the vehicle is not fitted with ramp detection devices, alternative methods should be identified to distinguish between flat and ramp conditions, ensuring that their controls do not conflict.

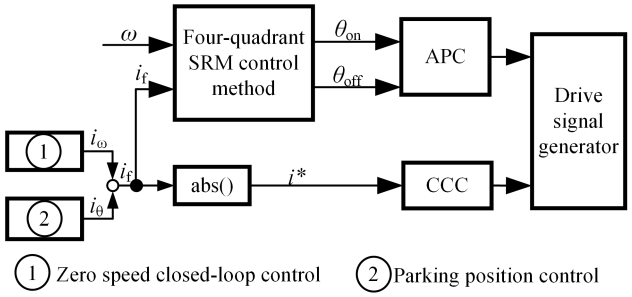

FIGURE 9. Composition of the system drive signal.

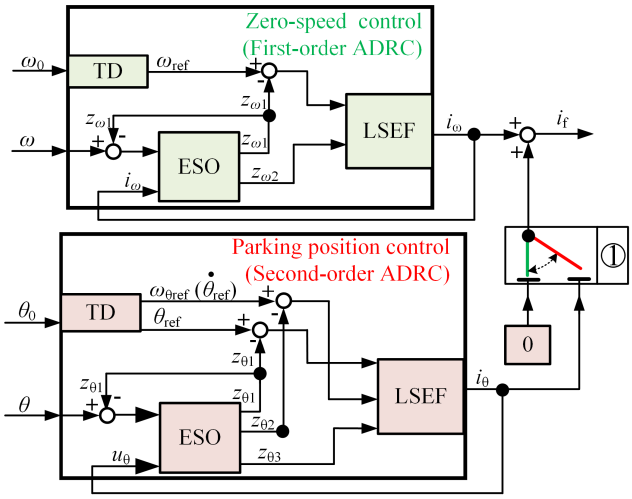

FIGURE 10. ADRC block diagram of the system.

B. DESIGN OF OPTIMIZED PARKING CONTROL

Since the parking brake system needs to identify parking conditions and requires high reliability, two active disturbance rejection controllers (ADRCs) are used to achieve the smooth switch from zero-speed control to parking position control. As shown in Fig. 9, the final current chopping control (CCC) value (i^*) consists of i_ω and i_θ, which represent the magnitudes of control values for zero-speed control and parking position control, respectively. The i_ω is the most crucial factor in vehicle dynamic driving and parking control, while i_θ is only activated under specific parking control conditions. Otherwise, i_θ will be set to 0. Fig. 10 shows the block diagrams of two control methods, using first-order and second-order ADRCs. i_f is the sum of i_ω and i_θ. Although both i_ω and i_θ collectively influence i_f, under the parking position control, the speed variation is minimal, resulting in little change in i_ω. At this point, i_θ plays a crucial role in position control, indicating that i_ω and i_θ are relatively independent output of subsystems. The relevant expressions and designs are as follows.

1) ZERO-SPEED CONTROL

To ensure the dynamic performance of the SRM and provide disturbance observation for judging the T_i, a first-order

active disturbance rejection controller is used for the speed closed-loop control of the system. (4), (5), and (6) show the tracking differentiator (TD), extended state observer (ESO) and linear state error feedback (LSEF) inside the controller, respectively. For (4), where *fhan*() is the discrete-time optimal control algorithm (detailed expression is shown in appendix), h is the sampling period for the system, r_ω is the speed factor, and ω_0 is the target speed. For (5), where $z_{\omega 1}$ and $z_{\omega 2}$ estimate actual angular velocity and disturbance by ESO, respectively. β_{04} and β_{05} are adjustable parameters. For (6), where $i_{\omega 1}$ and $-z_{\omega 2}/b_0$ are linear error feedback and compensation amount of all system disturbances, respectively.

2) PARKING POSITION CONTROL

Considering the application of ADRC in servo control field, parking position control uses a second-order active disturbance rejection controller. (7), (8), and (9) show the TD, ESO and LSEF inside the controller, respectively. For (7), where h is the sampling period for the system, r_θ is the speed factor, and θ_0 is the target angle. For (8), where $z_{\theta 1}$, $z_{\theta 2}$ and $z_{\theta 3}$ are the estimations of actual angular position, velocity and disturbance by ESO, respectively. β_{01}, β_{02} and β_{03} are adjustable parameters. For (9), where $i_{\theta 1}$, $i_{\theta 2}$ and $-z_{\theta 3}/b_3$ are linear error feedbacks and compensation amount of all system disturbances, respectively.

$$\begin{cases} fh = fhan\left(\omega_{ref} - \omega_0, \dot{\omega}_{ref}, r_\omega, h\right) \\ \omega_{ref}(k+1) = \omega_{ref}(k) + h^*\dot{\omega}_{ref}(k) \\ \dot{\omega}_{ref}(k+1) = \dot{\omega}_{ref}(k) + h^*fh \end{cases} \tag{4}$$

$$\begin{cases} e_\omega(k) = z_{\omega 1}(k) - \omega(k) \\ z_{\omega 1}(k+1) = z_{\omega 1}(k) + h * (z_{\omega 2}(k) - \beta_{04}e_\omega(k) + b_0 u) \\ z_{\omega 2}(k+1) = z_{\omega 2}(k) - h * \beta_{05} * e_\omega(k) \end{cases} \tag{5}$$

$$\begin{cases} e_{\omega 1} = \omega_{ref} - z_{\omega 1} \\ i_{\omega 1} = \beta_3 * e_{\omega 1} \\ i_\omega = i_{\omega 1} - z_{\omega 2}/b_0 \end{cases} \tag{6}$$

$$\begin{cases} fh = fhan\left(\theta_{\text{ref}} - \theta_0, \dot{\theta}_{\text{ref}}, r_\theta, h\right) \\ \theta_{\text{ref}}(k+1) = \theta_{\text{ref}}(k) + h^*\dot{\theta}_{\text{ref}}(k) \\ \dot{\theta}_{\text{ref}}(k+1) = \dot{\theta}_{\text{ref}}(k) + h^*fh \end{cases} \tag{7}$$

$$\begin{cases} e_\theta(k) = z_{\theta 1}(k) - \theta(k) \\ z_{\theta 1}(k+1) = z_{\theta 1}(k) + h * (z_{\theta 2}(k) - \beta_{01}e_\theta(k)) \\ z_{\theta 2}(k+1) = z_{\theta 2}(k) + h * (z_{\theta 3}(k) - \beta_{02}e_\theta(k) + b_3 u) \\ z_{\theta 3}(k+1) = z_{\theta 3}(k) - h * \beta_{03} * e_\theta(k) \end{cases} \tag{8}$$

$$\begin{cases} e_{\theta 1} = \theta_{ref} - z_{\theta 1} \\ e_{\theta 2} = \dot{\theta}_{ref} - z_{\theta 2} \\ i_{\theta 1} = \beta_1 * e_{\theta 1} \\ i_{\theta 2} = \beta_2 * e_{\theta 2} \\ i_\theta = i_{\theta 1} + i_{\theta 2} - z_{\theta 3}/b_3 \end{cases} \tag{9}$$

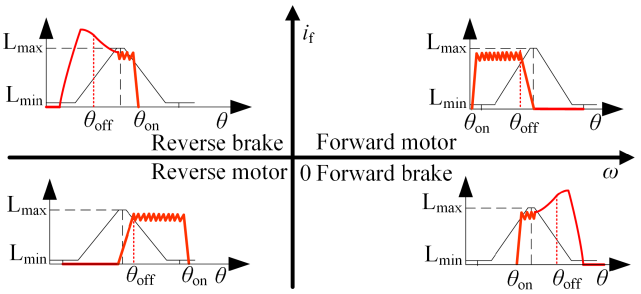

FIGURE 11. Four-quadrant SRM drive method.

3) FOUR-QUADRANT SRM DRIVE METHOD

According to the requirements of electric vehicles for SRM motoring and braking, as the critical parameters of angle position control (APC), the turn-on angle position (θ_{on}) and turn-off angle position (θ_{off}) are determined by a four-quadrant SRM drive method. As shown in Fig. 11, i_{f} and ω are used as the basis for specific operating quadrants. This method helps restrain the impact torque of a conventional four-quadrant SRM drive caused by the constant current amplitude of the conduction interval during the motoring and braking switching process. Since the speed of the parking position control process is close to $0°/s$, the θ_{on} and θ_{off} correspond to the minimum and maximum inductance according to the actual four-quadrant operating region.

C. REALIZATION OF OPTIMIZED PARKING CONTROL

In order to realize the optimized parking control, in addition to the implementation of **Step 1** and **Step 2**, further research needs to be investigated under both parking conditions (ramp & flat).

1) PARKING ON THE RAMP

According to the optimized parking control shown in Fig. 7, when the vehicle is in an upward attitude and receives a parking order, the zero-speed control is engaged, and the rotor begins to decelerate to $\omega = 0°/s$.

By identifying the $z_{\omega 2}$, the vehicle's attitude can be judged. For the upward attitude in Fig. 10, $z_{\omega 2} < 0$. Then the θ_0 can be determined, and **Step 2** works. The rotor moves along the T_{i} according to the trend shown in Fig. 12(a). Any rotor angles after **Step 1** are all within the regulated range.

Since the ideal parking region exists, the overshoot moving towards θ_{m} is permitted. As shown in Fig. 12(b), to avoid the change of speed direction (stemming from (2) and (3)) due to minor overshoot, all angles within the ideal parking region are treated as θ_0, effectively circumventing polarity changes in angle error. Building upon the parking stability analysis, it is demonstrated that the rotor, even when entering the ideal parking region at a low initial speed, can achieve self-stabilization without the need to modify the regulator value.

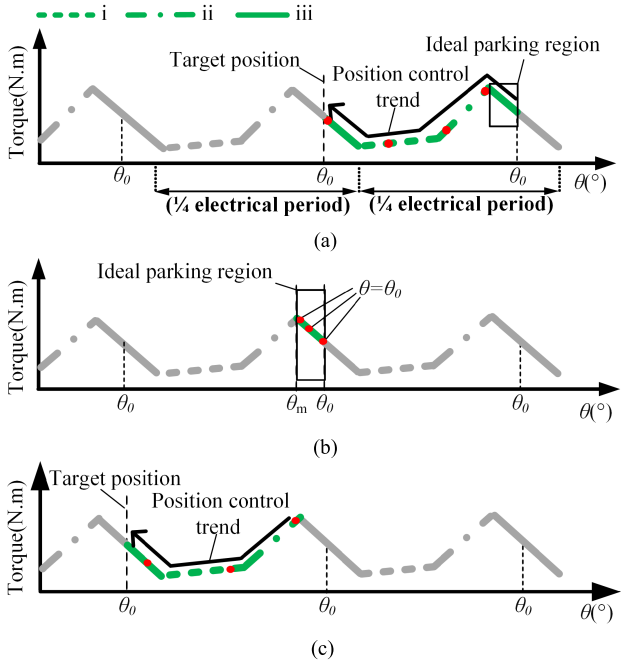

FIGURE 12. Optimized parking control for parking on the ramp. (a) Description of position control trend after zero-speed control. (b) Definition for rotor angles in ideal parking region. (c) Description of position control trend after θ exceeds the ideal parking region.

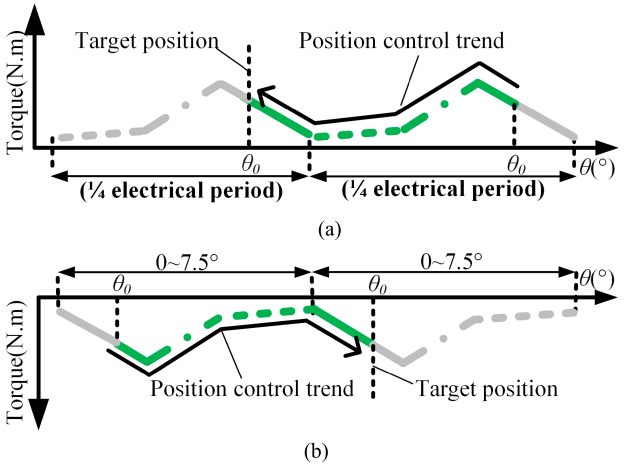

FIGURE 13. Optimized parking control for parking on the flat. (a) $T_e > 0$. (b) $T_e < 0$.

If the initial speed of the rotor entering the ideal parking region is too high, the rotor will move to the next target value (θ_0) in the direction shown in Fig. 12(c).

If the speed of the rotor is too high after **Step 1**, as shown in Fig. 7, the system will initialize the parameters of parking position control and re-enter the zero-speed control.

The optimized parking control with a downward attitude is similar to the above realization. After **Step 1**, the disturbance observed by the ESO results in $z_{\omega 2} > 0$. The θ_0 and the position control trend will be adjusted accordingly.

TABLE 1. Key parameters of experimental test.

Parameters	Value
Vehicle Model	Electric Forklift
Weight & Moment of Inertia	3030kg & 0.283kg·m^2
Gear Ratio	26.5:1
Coefficient of Rolling Resistance	0.0282
Ramp Slope	15%
Rated Power & Voltage	9kW & 48V
Rated Speed & Torque	1000r/min & 86N.m
θ_m,θ_n (Refer to Fig.4)	5.8°,6.5°
θ_m,θ_n (Refer to Fig.4)	1.7°,1°

2) PARKING ON THE FLAT

Different from the ramp, there is no T_i on the flat. The T_e must be used to balance the T_f. i^* cannot be decreased to 0A through the zero-speed control since the speed error is 0°/s after **Step 1**. That is why there is still power consumption when the vehicle is fully parked. As "$i_f = i_\omega + i_\theta$" is known, i_θ can be used to offset i_ω. Hence, i_f can gradually approaches 0, the system can finally achieve no power consumption stationary. As shown in Fig. 13, same as parking on the ramp, $z_{\omega 2}$ determines the trend of parking position control, and accordingly, θ_0 can also be determined. According to (7), (8) and (9), the further design is as follows:

1) When $z_{\omega 2} < 0$, then $e_{\theta 1} < 0$, $e_{\theta 2} < 0$, $e_\theta = 0$. Due to the influence of TD in (7), i_θ does not have a sudden change, and it satisfies ≤ 0.
2) When $z_{\omega 2} \geq 0$, then $e_{\theta 1} > 0$, $e_{\theta 2} > 0$, $e_\theta = 0$. Due to the influence of TD in (7), i_θ will not have a sudden change, and it satisfies ≥ 0.

Due to the design, the control method does not change the rotor angle after **Step 1**, and i_f eventually approaches 0. At this time, by limiting the polarity of i_f, ensuring that the polarity of i_f does not modify, $i_f = 0$ can be made, corresponding to $i* = 0$ in Fig. 8, the system can finally achieve no power consumption on the flat.

D. SUMMARY OF OPTIMIZED PARKING CONTROL

With the addition of a polarity restriction for "parking on the flat," there is no conflict between the methods for parking on flat and ramp. By adjusting i_f and rotor angle, "parking on the ramp" optimizes power consumption. Furthermore, "parking on the flat" achieves zero power consumption while stationary by making the control value (i_f) tend to 0 through angle error. This outcome is in line with the original goal of the study.

IV. SIMULATION VERIFICATION

To validate the feasibility and effectiveness of the proposed control method. The parking model (see Fig. 14) for a four-phase 16/12 SRM drive system is implemented in MATLAB/SIMULINK with the system parameters in TABLE 1. Moreover, the relevant system parameters are shown in TABLE 1. The angle length of the ideal parking region is set as 0.7° shown in Fig. 3. Through the finite element

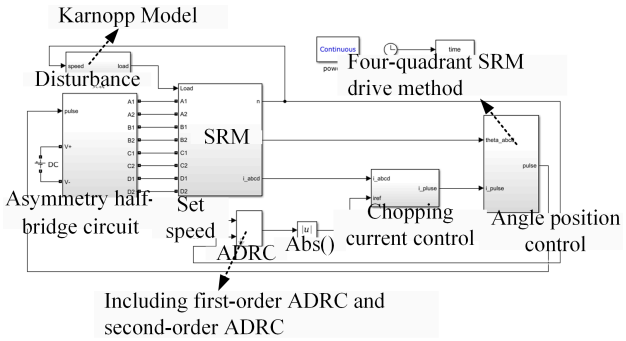

FIGURE 14. Structure of parking simulation module.

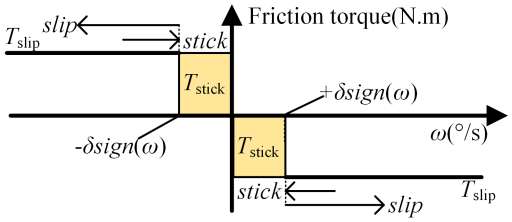

FIGURE 15. Karnopp Model ignoring viscous friction and Stribeck effect.

simulation, the exact region division is defined as shown in Fig. 3. For $T_e > 0$, region i, ii, iii are divided as $0° \sim 4.1°$, $4.1° \sim 5.8°$, $5.8° \sim 7.5°$, respectively. For $T_e < 0$, region i, ii, iii are divided as $3.4° \sim 7.5°$, $1.7° \sim 3.4°$, $0° \sim 1.7°$, respectively.

A. ANALYSIS OF KARNOPP MODEL

To simplify the analysis, some special sliding friction models can be introduced to analyze the parking model. Karnopp Model switches states by detecting zero speed, which can reflect the system's dynamic and static friction change process during model establishment [29]. The Karnopp model in this paper is shown in Fig. 15. Ignoring viscous friction and the Stribeck effect, T_{slip} and T_{stick} in Fig. 15 are dynamic friction torque and static friction torque, respectively. δ is the critical angular velocity (ω), $°/s$, $\delta > 0°/s$. The relationship between T_f, T_{slip}, T_{stick}, δ and ω is:

$$T_f = \begin{cases} T_{stick}, & |\omega| \le \delta \\ T_{slip}, & |\omega| > \delta \end{cases} \tag{10}$$

At the same time, T_e, T_i, T_{slip}, T_{stick} shall meet:

$$\begin{cases} |T_i| = Gr \sin a/i_g \\ T_{stick} = -(T_e + T_i) \\ T_{slip} = -\text{sign}(\omega) f_r r G \cos a/i_g \\ \{|T_{stick}|\}_{max} = |T_{slip}| \end{cases} \tag{11}$$

As shown in (11), the direction of T_f shall be determined according to the rotation direction or trend of rotation, which plays an essential role in the simulation analysis of this paper. According to the application of the model, "δ =0.01°/s" is set.

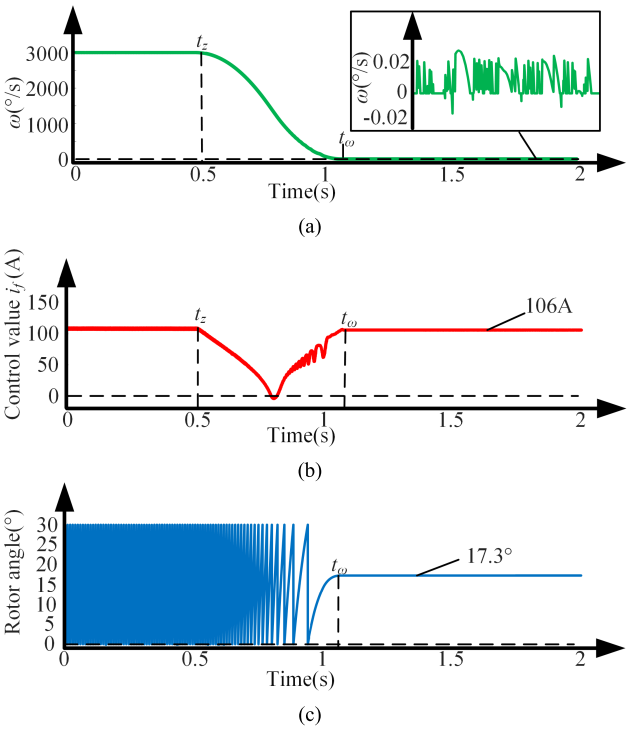

FIGURE 16. Simulation of the method without parking position control on the ramp. (a) Angular speed variations. (b) Control value variations. (c) Rotor angle variations.

B. VERIFICATION OF THE METHOD WITHOUT PARKING POSITION CONTROL FOR PARKING ON THE RAMP

As shown in Fig. 16, the vehicle travels on the ramp with an upward posture at an angular speed of 3000°/s (1000r/min). The system receives the parking order at time t_z, and enters the zero-speed control, finally completes the parking process at time t_ω. It can be seen from Fig. 16(c), the fully parked rotor angle is 17.3°. As the rotor angle is in the region i analyzed in Fig. 4, the fully parked rotor angle is not only in the region of low power efficiency but also in the region of terrible stability. Fig. 16(a) shows that the rotor tends to rotate in the positive direction in the final parking state due to the direction of rolling resistance torque (T_f), which is opposite to the direction of grade resistance torque (T_i). As a result, T_e, T_i and T_f satisfy (2), which means that power consumption is not allowed from this perspective.

Since the ripple of the rolling resistance torque (T_f) is larger than the electromagnetic torque variation, the system can still maintain a stationary parking state in region i (similar current waveforms can be seen in Fig. 19). Moreover, parts of the instantaneous angular velocity from the Karnopp model exceed 0.01°/s after t_ω in Fig. 16(a), and the rotor angle in Fig. 16(c) changes very little within 1s. Therefore, it can be considered that the stationary parking state has been achieved.

C. VERIFICATION OF THE METHOD WITH PARKING POSITION CONTROL FOR PARKING ON THE RAMP

According to the optimized parking method in Fig. 7, as shown in Fig. 17, the system enters parking position control

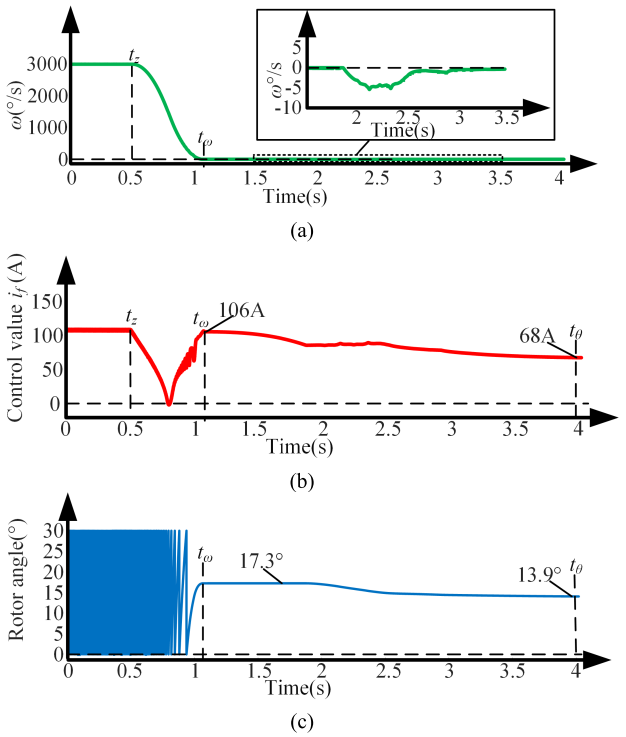

FIGURE 17. Simulation of the method with parking position control on the ramp. (a) Angular speed variations. (b) Control value variations. (c) Rotor angle variations.

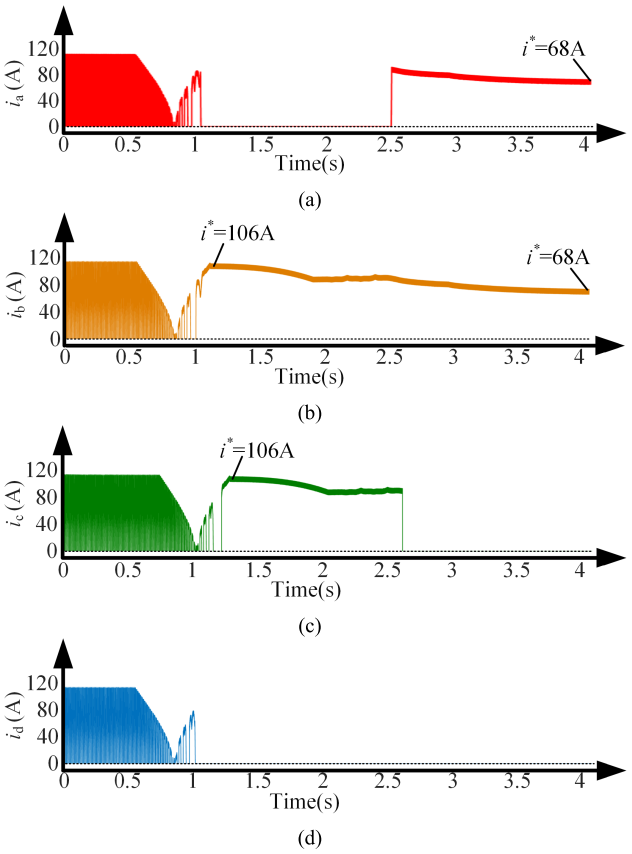

FIGURE 18. Current variations of each phase. (a) Phase A. (b) Phase B. (c) Phase C. (d) Phase D.

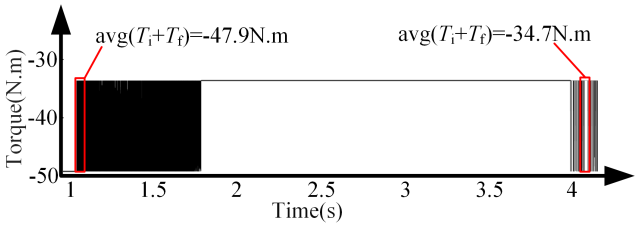

FIGURE 19. Variations of ($T_i + T_f$) through the parking process.

after t_ω. The rotor angle at time t_ω is 17.3°, at the same time, $z_{\omega 2} < 0$. According to the definition of the ideal parking region in Table 1, θ_0 is defined as 14° (6.5°+ 7.5°) in this condition. Based on the parking position control, the control value (i_f) gradually approaches 0, the rotor moves to the ideal parking position region, and the rotor finally achieves stationary parking at 13.9° (in ideal parking region). The four phases current are shown in Fig.18.

In addition to moving the rotor to ideal parking region, the position control process in Fig. 12 also aims to ensure that the direction of angular velocity is consistent with the direction of T_i during the parking position control, which means that the direction of T_f is consistent with the direction of T_e. Fig. 19 shows the change of ($T_f + T_i$), while the direction of T_f satisfies (3) when rotor angle is at 13.9°. As shown in Fig. 17, the system's power consumption has been further optimized.

D. VERIFICATION OF THE METHOD WITHOUT PARKING POSITION CONTROL FOR PARKING ON THE FLAT

As shown in Fig. 20, the vehicle travels on the flat with an upward posture at an angular speed of 3000°/s (1000r/min). The system receives the parking order at time t_z, and enters the zero-speed control, finally completes the parking process at time t_ω. The final control value (i_f) and rotor angle in final parking state are −12.9A and 4.2°, respectively. As can be seen in Fig. 20(a), although there is no grade resistance torque (T_i), the electromagnetic torque (T_e) of the system is used to balance the rolling resistance torque (T_f). Since the angular speed is almost 0°/s under the final parking state, the control value (i_f) calculated by zero-speed control cannot be further changed by speed error. It is difficult for the system to achieve no power consumption stationary on the flat.

E. VERIFICATION OF THE METHOD WITH PARKING POSITION CONTROL FOR PARKING ON THE FLAT

According to the optimized parking method in Fig. 7, as shown in Fig. 21, the system enters parking position control after t_ω. The rotor angle at time t_ω is 4.2°, at the same time, $z_{\omega 2} > 0$. According to the definition of the ideal parking region in Table 1, θ_0 is defined as 8.5° (1°+ 7.5°) in this condition. Based on the parking position control, although the rotor angle does not move, $z_{\omega 2} \geq 0$, then $e_{\theta 1} > 0$, $e_{\theta 2} > 0$. Therefore, the control value (i_f) gradually approaches 0.

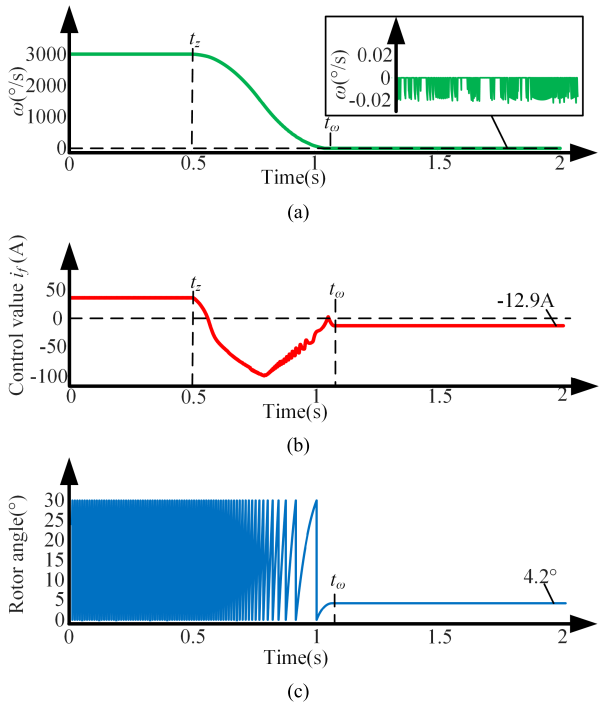

FIGURE 20. Simulation of the method without parking position control on the flat. (a) Angular speed variations. (b) Control value variations. (c) Rotor angle variations.

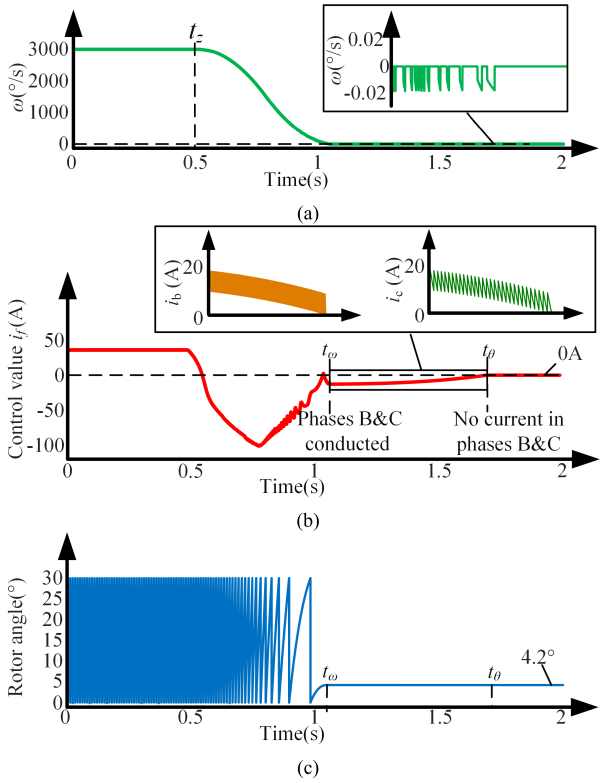

FIGURE 21. Simulation of the method with parking position control on the flat. (a) Angular speed variations. (b) Control value variations. (c) Rotor angle variations.

By limiting the change of polarity of the control value (i_f), in Fig. 21(a) and Fig. 21(b), the control value (i_f) finally approaches 0, and the phase current decreases to 0A, and the rotor does not tend to move in the negative direction. The system achieves no power consumption stationary on the flat.

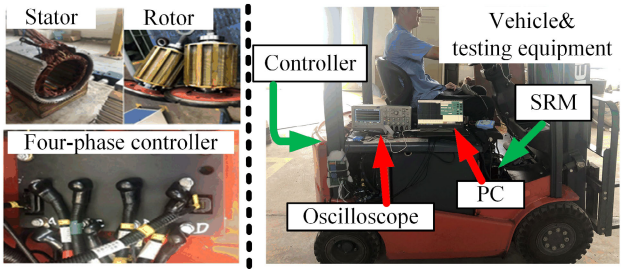

FIGURE 22. Experimental setup.

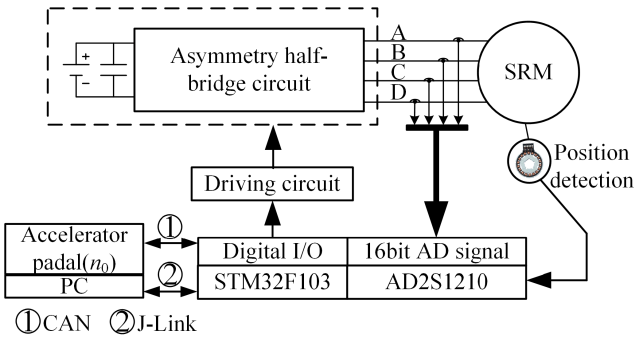

FIGURE 23. System topology and signal acquisition.

V. EXPERIMENTAL VERIFICATION

To validate the feasibility and effectiveness of the proposed control method experimentally. An experimental system has been set up with system parameters, also shown in TABLE 1.

The experimental system is shown in Fig. 22. The four-phase controller is located at the rear of the forklift, covered by a bob-weight. The forklift is a front-drive design with the SRM under the driver's foot. As shown in Fig. 23, an asymmetry half-bridge circuit is used in the system power topology. The proposed control methods are implemented in an STM32F103 (Electronic Control Unit, ECU) control board, and AD2S1210 resolves the position signal. In addition to the analogue signal formed by the current sensor entering the ECU, the four-phase current is presented through an external current acquisition circuit through an oscilloscope. The CAN J1939 protocol communicates any operation signal of the driver to the vehicle. The J-Link can record required parameters in ECU.

A. VERIFICATION OF THE METHOD WITH OR WITHOUT PARKING POSITION CONTROL FOR PARKING ON THE RAMP

Comparative experimental tests with the same ramps are carried out. Fig. 24 shows the experimental results of the vehicle for parking on the ramp only by zero-speed control. Although the ramps of the four tests are the same, the rotor angle (θ) and control value (i_f) are random in the final parking

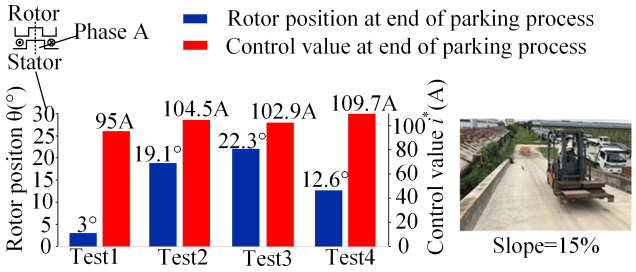

FIGURE 24. Experimental test of the parking brake system only with zero-speed control for parking on the ramp.

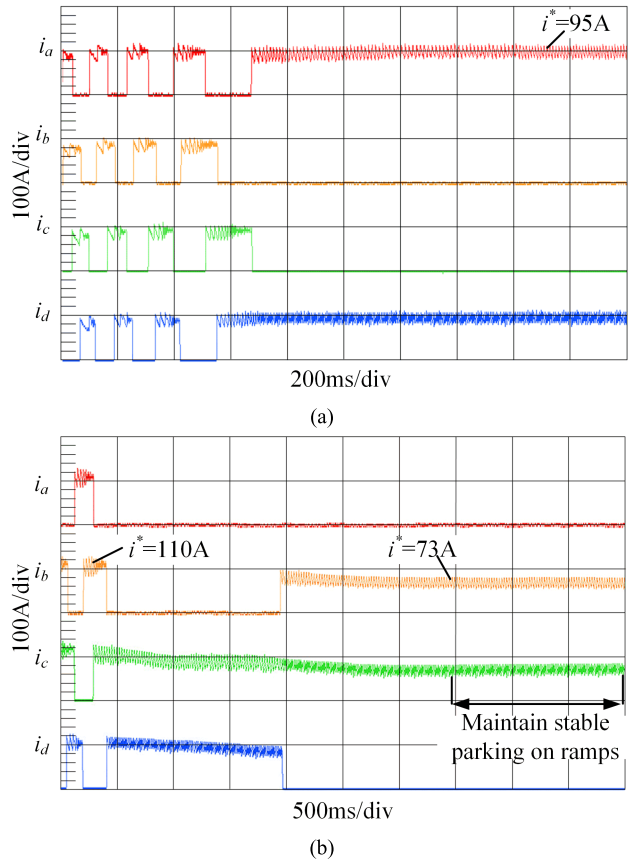

FIGURE 25. Current variations of each phase. (a) Parking brake system only with zero-speed control. (b) Parking brake system with zero-speed and parking position controls.

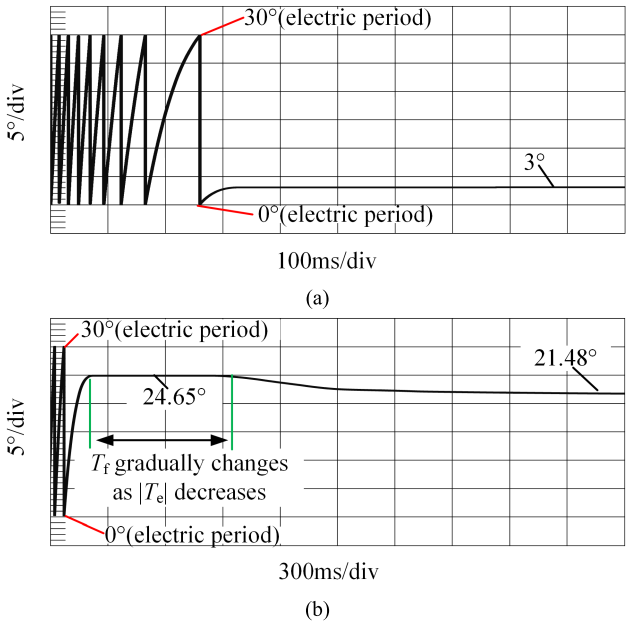

FIGURE 26. Variations of rotor angle. (a) Parking brake system only with zero-speed control. (b) Parking brake system with zero-speed and parking position controls.

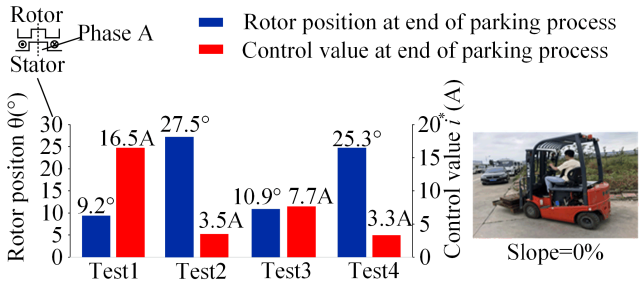

FIGURE 27. Experimental test of the parking brake system only with zero-speed control for parking on the flat.

stationary state, which is to the analysis results of section II on the static torque-angle characteristic and T_f. Fig. 25(a) and Fig. 26(a) show the four phases current and rotor angle of Test 1, respectively. It can be seen that the rotor angle is in region i, and the direction of T_f is unknown. With the optimized parking control in Fig. 7, as shown in Fig. 25(b) and Fig. 26(b), the system enters parking position control after the preliminary realization of zero-speed control. The rotor angle initially stays at 24.65°, at the same time, $z_{\omega 2} < 0$. Due to the definition of the ideal parking region in Table 1, θ_0 is defined as 21.5° (6.5°+2· 7.5°) in this condition.

The final results indicate that the phase current is reduced from an initial 110A to 73A. Considering the measured value of a single-phase (10mΩ), the power savings surpass 100W when two phases are conducted. The rotor's position shifts from its initial 24.65° to 21.48°, facilitating the control of the rotor from region i to the ideal parking region. Consequently, the parking stability is further optimized.

B. VERIFICATION OF THE METHOD WITH OR WITHOUT PARKING POSITION CONTROL FOR PARKING ON THE FLAT

Comparative experimental tests with same flats are carried out. Fig. 27 shows the experimental results of the vehicle for parking on the flat only by zero-speed control. Although the flats of the four tests are the same, rotor angle (θ) and control value (i_f) are random in fully parked. Due to the static torque-angle characteristic and T_f. Fig. 28(a) and Fig. 29(a) show the four phases current and the rotor angle of Test 1, respectively. Although the final rotor angle (9.2°) is in region i, the rotor angle within this region is not a critical consideration for flat

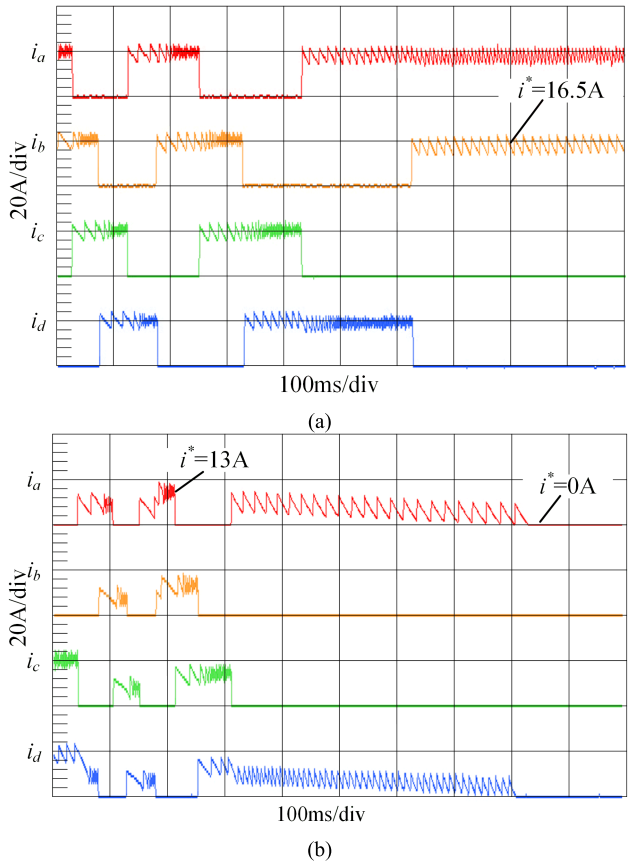

FIGURE 28. Current variations of each phase. (a) Parking brake system only with zero-speed control. (b) Parking brake system with zero-speed and parking position controls.

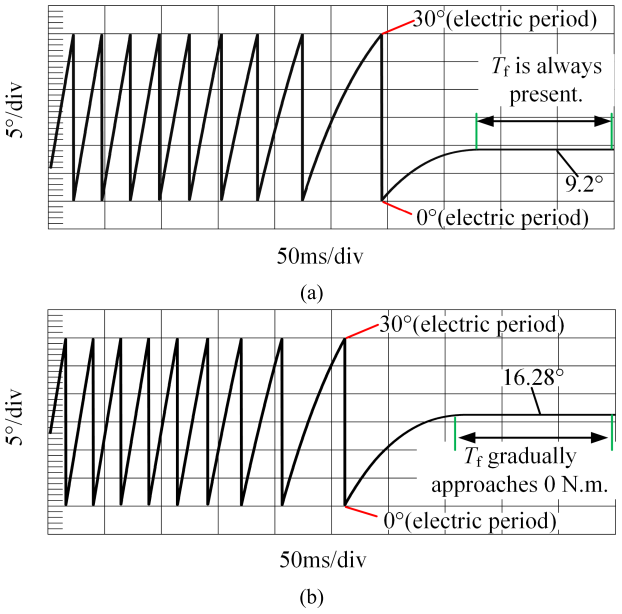

FIGURE 29. Variations of rotor angle. (a) Parking brake system only with zero-speed control. (b) Parking brake system with zero-speed and parking position controls.

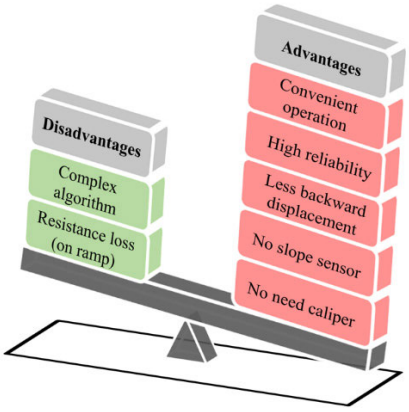

FIGURE 30. Advantages and disadvantages of optimized parking method compared with conventional methods.

parking. The issue to be addressed is the current in the phase winding (16.5A) observed in the final parking state, as shown in Fig. 19(a).

With the optimized parking control in Fig. 7, as shown in Fig. 28(b) and Fig. 29(b), the system enters parking position control after the preliminary realization of zero-speed control. The rotor angle initially stays at 16.28° (region iii), $z_{\omega 2} > 0$. Due to the definition of the ideal parking region in Table 1, θ_0 is defined as 23.5° (1°+3·7.5°) in this condition. Based on the parking position control, although the rotor angle does not move, $z_{\omega 2} \geq 0$, then $e_{\theta 1} > 0$, $e_{\theta 2} > 0$. Therefore, the control value (i_f) gradually approaches 0. By limiting the change of polarity of i_f, as shown in Fig. 28(b) and Fig. 29(b), the rotor does not move. At the same time, the phase current still decreases to 0A. System finally achieves no power consumption stationary on the flat.

VI. DISCUSSION AND FUTURE WORK

Based on the experimental test results, the optimized parking method successfully achieves the objectives of parking on both ramps and flats. By comparing the summary of the conventional vehicle parking system provided in the Introduction, Fig. 30 illustrates the main advantages and disadvantages of the optimized parking method. Specifically, the system can enter an automatic parking control process upon receiving the parking order, while conventional parking methods require additional equipment to achieve similar parking effects. Therefore, the optimized parking method proposed in this study holds significant practical value in the field of SRM for Electric Vehicles (EVs) and Hybrid Electric Vehicles (HEVs). On this basis, in the future, it is crucial to further optimize the parking strategies for SRM and caliper systems, as well as explore diverse topology structures of SRM for parking control applications.

VII. CONCLUSION

This paper presents an optimized parking control method for electric vehicle solely depending on the switched reluctance drive motor. By optimizing the final rotor angle and

TABLE 2. Parameters of first-order & second-order ADRC.

Parameters	Value	Parameters	Value
r_ω	6000	h	0.001
β_{04}	500	β_{05}	3500
β_3	17	b_0	20
r_θ	5	h	0.001
β_{01}	60	β_{02}	80
β_{03}	3000	b_3	20
β_1	90	β_2	20

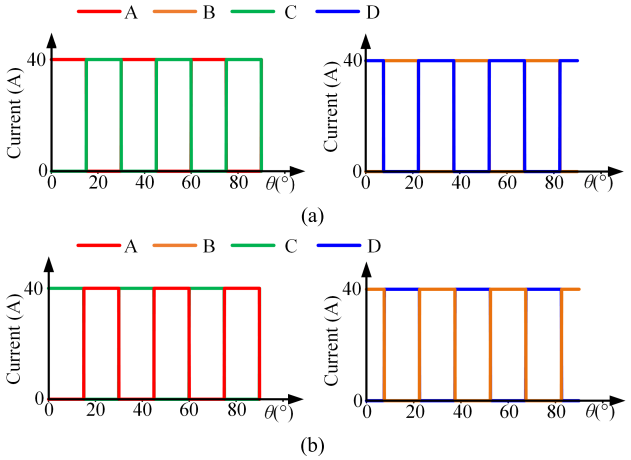

FIGURE 31. Simulated currents that generate the torque of 40A. (a) $T_e > 0$. (b) $T_e < 0$.

combining the zero-speed control and parking position control through ADRC, both the stability and power consumption economy of the parking process are improved. The working principle and realization of the proposed control method have been introduced in detail for parking on both ramps and flats. Simulation and experimental results on a practical electric vehicle prove the proposed method's merits in both stability and economy.

APPENDIX

As shown in Fig. 10, the parameters of ADRC in the simulation and experimental test are shown in TABLE 2.

Fig.31 shows the simulated currents that generate the torque curves depicted in Fig.3 at 40A, with the torque curves at 70A and 100A only varying in current amplitude while the driving logic remains unchanged.

As widely used in the TD of ADRC, the expression of *fhan* algorithm is presented as follow.

$$
\begin{aligned}
fh &= fhan(\xi_1, \xi_2, r, h) \\
&= \begin{cases} d = rh, d_0 = hd, y = \xi_1 + h\xi_2 \\ a_0 = \sqrt{d^2 + 8r\,|y|} \\ a = \begin{cases} \xi_2 + \dfrac{(a_0 - d)}{2} sign(y) & |y| > d_0 \\ \xi_2 + \dfrac{y}{h} & |y| \le d_0 \end{cases} \\ fhan = -\begin{cases} rsign(a) & |a| > d \\ r\dfrac{a}{d} & |a| \le d \end{cases} \end{cases}
\end{aligned} \tag{12}
$$

COMPETING INTERESTS

The authors declare that they have no competing interests.

REFERENCES

[1] N. Bagheri and H. Alipour, "Yaw rate control and actuator fault detection and isolation for a four wheel independent drive electric vehicle," *J. Operation Autom. Power Eng.*, vol. 5, no. 1, pp. 83–95, Jun. 2017.

[2] L. Wu, H. Wang, D. Pi, E. Wang, and X. Wang, "Hill-start of distributed drive electric vehicle based on pneumatic electronic parking brake system," *IEEE Access*, vol. 8, pp. 64382–64398, 2020.

[3] M. Paul, K. Baidya, and R. Deepak, "Electromagnetic parking brake system for electric vehicles," SAE, Warrendale, PA, USA, Tech. Paper 2019-26-0119, 2019.

[4] C. Crover, I. Knight, F. Okoro, I. Simmons, G. Couper, P. Massie, and B. Smith, "Automated emergency brake systems: Technical requirements, cost and benefits," DG Enterprise, Eur. Commission, TRL Limited, Crowthorne, U.K., Project Rep. PPR227, version 1.1, Apr. 2008.

[5] G.-H. Park, S.-S. Lee, S.-K. Kim, M.-K. Jung, and H.-H. Kang, "Automatic restarting methods of electric forklifts in the free running state," in *Proc. World Electric Vehicle Symp. Exhib. (EVS)*, Nov. 2013, pp. 1–8.

[6] T. Lin, Q. Wang, B. Hu, and W. Gong, "Development of hybrid powered hydraulic construction machinery," *Autom. Construction*, vol. 19, no. 1, pp. 11–19, Jan. 2010.

[7] M. Naruse, M. Tamsru, and K. Kimoto, "Hybrid construction equipment," U.S. Patent 6 708 787, Mar. 23, 2004.

[8] M. Ochiai, "Development for environment friendly construction machinery," *Construction*, vol. 9, pp. 24–28, Sep. 2003.

[9] Z. Yong, Z. Li-Yin, C. Ding-Chun, and Y. Hong, "The straight-line driving control strategy of the hybrid track-type bulldozer," in *Proc. 9th Int. Conf. Natural Comput. (ICNC)*, Shenyang, China, Jul. 2013, pp. 1702–1706.

[10] R. Madhavan and B. G. Fernandes, "Axial flux segmented SRM with a higher number of rotor segments for electric vehicles," *IEEE Trans. Energy Convers.*, vol. 28, no. 1, pp. 203–213, Mar. 2013.

[11] A. Chiba, Y. Takano, M. Takeno, T. Imakawa, N. Hoshi, M. Takemoto, and S. Ogasawara, "Torque density and efficiency improvements of a switched reluctance motor without rare-earth material for hybrid vehicles," *IEEE Trans. Ind. Appl.*, vol. 47, no. 3, pp. 1240–1246, May 2011.

[12] K. Kiyota and A. Chiba, "Design of switched reluctance motor competitive to 60-kW IPMSM in third-generation hybrid electric vehicle," *IEEE Trans. Ind. Appl.*, vol. 48, no. 6, pp. 2303–2309, Nov. 2012.

[13] J. D. Widmer, R. Martin, and B. C. Mecrow, "Optimization of an 80-kW segmental rotor switched reluctance machine for automotive traction," *IEEE Trans. Ind. Appl.*, vol. 51, no. 4, pp. 2990–2999, Jul. 2015.

[14] M. Abdalmagid, M. Bakr, and A. Emadi, "A linesearch-based algorithm for topology and generative optimization of switched reluctance machines," *IEEE Trans. Transport. Electrific.*, vol. 9, no. 3, pp. 3849–3866, Sep. 2023.

[15] L. Ge, J. Zhong, C. Bao, S. Song, and R. W. De Doncker, "Continuous rotor position estimation for SRM based on transformed unsaturated inductance characteristic," *IEEE Trans. Power Electron.*, vol. 37, no. 1, pp. 37–41, Jan. 2022.

[16] M. Kawa, K. Kiyota, J. Furqani, and A. Chiba, "Acoustic noise reduction of a high-efficiency switched reluctance motor for hybrid electric vehicles with novel current waveform," *IEEE Trans. Ind. Appl.*, vol. 55, no. 3, pp. 2519–2528, May 2019.

[17] H. Sobue, A. Chiba, Y. Cai, K. Kiyota, Y. Fujii, K. Senda, and S. Yoshizaki, "Analysis and experimental comparison of acoustic noise of three switched reluctance motors made of conventional steel, high silicon steel, and amorphous iron," *IEEE Trans. Ind. Appl.*, vol. 57, no. 6, pp. 5907–5915, Nov. 2021.

[18] J. Furqani, M. Kawa, C. A. Wiguna, N. Kawata, K. Kiyota, and A. Chiba, "Current reference selection for acoustic noise reduction in two switched reluctance motors by flattening radial force sum," *IEEE Trans. Ind. Appl.*, vol. 55, no. 4, pp. 3617–3629, Jul. 2019.

[19] C. Gan, J. Wu, Q. Sun, W. Kong, H. Li, and Y. Hu, "A review on machine topologies and control techniques for low-noise switched reluctance motors in electric vehicle applications," *IEEE Access*, vol. 6, pp. 31430–31443, 2018.

[20] A. K. Sahu, A. Emadi, and B. Bilgin, "Noise and vibration in switched reluctance motors: A review on structural materials, vibration dampers, acoustic impedance, and noise masking methods," *IEEE Access*, vol. 11, pp. 27702–27718, 2023.

[21] H. Kim, C. Nerse, J. Lee, and S. Wang, "Multidisciplinary analysis and multiobjective design optimization of a switched reluctance motor for improving sound quality," *IEEE Access*, vol. 7, pp. 66020–66027, 2019.
[22] W. Yan, H. Chen, S. Liao, Y. Liu, and H. Cheng, "Design of a low-ripple double-modular-stator switched reluctance machine for electric vehicle applications," *IEEE Trans. Transport. Electrific.*, vol. 7, no. 3, pp. 1349–1358, Sep. 2021.
[23] M. V. de Paula and T. A. d. S. Barros, "A sliding mode DITC cruise control for SRM with steepest descent minimum torque ripple point tracking," *IEEE Trans. Ind. Electron.*, vol. 69, no. 1, pp. 151–159, Jan. 2022.
[24] B. Jing, X. Dang, Z. Liu, and S. Long, "Torque ripple suppression of switched reluctance motor based on fuzzy indirect instant torque control," *IEEE Access*, vol. 10, pp. 75472–75481, 2022.
[25] D. F. Valencia, R. Tarvirdilu-Asl, C. Garcia, J. Rodriguez, and A. Emadi, "Vision, challenges, and future trends of model predictive control in switched reluctance motor drives," *IEEE Access*, vol. 9, pp. 69926–69937, 2021.
[26] S. Wang, Z. Hu, and X. Cui, "Research on novel direct instantaneous torque control strategy for switched reluctance motor," *IEEE Access*, vol. 8, pp. 66910–66916, 2020.
[27] L. Ge, J. Zhong, J. Huang, N. Jiao, S. Song, and R. W. De Doncker, "A novel model predictive torque control of SRMs with low measurement effort," *IEEE Trans. Ind. Electron.*, vol. 70, no. 4, pp. 3561–3570, Apr. 2023.
[28] X. Zhang, Q. Yang, M. Ma, Z. Lin, and S. Yang, "A switched reluctance motor torque ripple reduction strategy with deadbeat current control and active thermal management," *IEEE Trans. Veh. Technol.*, vol. 69, no. 1, pp. 317–327, Jan. 2020.
[29] L. R. Shirazi and A. Besançon-Voda, "Robust friction compensation based on karnopp model," in *Proc. Eur. Control Conf. (ECC)*, Sep. 2001, pp. 2558–2563.

PEILIN LIU received the B.Eng. degree in automation from the Chengxian College, Southeast University, Nanjing, China, in 2015, and the M.S. degree in electrical engineering from Shanghai Dianji University, Shanghai, China, in 2018. He is currently pursuing the Ph.D. degree in electrical engineering with the Nanjing University of Aeronautics and Astronautics, Nanjing, China. His research interest includes high-efficiency switched reluctance motor drive systems for automotive, renewable energy, and especially the control strategy of automotive SRM.

TAO WANG (Member, IEEE) was born in Dazhou, China. He received the B.Eng. and Ph.D. degrees from the College of Electrical Engineering, Zhejiang University, Hangzhou, China, in July 2013 and June 2018, respectively. From 2018 to 2020, he was a Postdoctoral Research Associate with the Department of Electronic and Electrical Engineering, The University of Sheffield, Sheffield, U.K. Since 2020, he has been with the Nanjing University of Aeronautics and Astronautics, Nanjing, China, where he is currently an Associate Professor with the College of Automation Engineering. His current research interests include wind power generation, aviation power supply, permanent magnet synchronous machine control, and model predictive control.

ZHIYUAN CHAI received the B.S. and M.S. degrees in electrical engineering from the Nanjing University of Aeronautics and Astronautics, Nanjing, China, in 2020 and 2023, respectively, where he is currently pursuing the Ph.D. degree in electrical engineering. His research interest includes high-efficiency switched reluctance machine drive systems for automotive, renewable energy, and especially integrated starter and generator (ISG) HEV systems.

CHUANG LIU was born in Anhui, China, in 1973. He received the B.S. degree in electrical engineering from Yanshan University, Qinhuangdao, China, in 1994, and the M.S. and Ph.D. degrees in electrical engineering from the Nanjing University of Aeronautics and Astronautics, Nanjing, China, in 1997 and 2000, respectively. In 2000, he was a Postdoctoral Researcher with the Nanjing University of Aeronautics and Astronautics. In 2002, he joined the Department of Electrical Engineering, Nanjing University of Aeronautics and Astronautics, where he has been a Professor with the Department of Electrical Engineering, College of Automation Engineering, since 2008. His research interests include permanent-magnet synchronous motors and switched reluctance motors for automotive, renewable energy, and aerospace applications.

XUEZHONG ZHU was born in Changzhou, China, in 1968. He received the B.S. and M.S. degrees in electrical engineering from the Nanjing University of Aeronautics and Astronautics, Nanjing, China, in 1992 and 1995, respectively. Since 1998, he has been an Adjunct Professor with the Department of Electrical Engineering, College of Automation Engineering, Nanjing University of Aeronautics and Astronautics. His research interest includes switched reluctance motors for aerospace applications, renewable energy, and power converter.